



# Regulation and mechanism study of the CoS<sub>2</sub>/Cu<sub>2</sub>S-NF heterojunction as highly-efficient bifunctional electrocatalyst for oxygen reactions

Wanqing Li<sup>a,b</sup>, Lei Wu<sup>a</sup>, Xiaochao Wu<sup>a</sup>, Chuan Shi<sup>a</sup>, Yongliang Li<sup>a,\*</sup>, Lei Zhang<sup>a</sup>, Hongwei Mi<sup>a</sup>, Qianling Zhang<sup>a</sup>, Chuanxin He<sup>a</sup>, Xiangzhong Ren<sup>a,\*</sup>

<sup>a</sup> College of Chemistry and Environmental Engineering, International Joint Research Center for Molecular Science, Shenzhen University, Shenzhen, Guangdong 518060, PR China

<sup>b</sup> Key Laboratory of Optoelectronic Devices and Systems of Ministry of Education and Guangdong Province, College of Physics and Optoelectronic Engineering, Shenzhen University, Shenzhen 518060, PR China

## ARTICLE INFO

### Keywords:

Bifunctional electrocatalyst  
Self-supporting electrode  
Carbon nanofiber  
Solid state batteries

## ABSTRACT

The precise design and controllable manufacture of electrocatalysts for efficient oxygen reactions (OER and ORR) based on the abundant elements of the earth are urgently required but challenging task. In this study, a CoS<sub>2</sub>/Cu<sub>2</sub>S heterostructured composite (CoS<sub>2</sub>/Cu<sub>2</sub>S-NF) supported by the porous carbon nanofibers is synthesized as a high-efficiency oxygen reaction electrocatalyst. As indicated from in-situ characterization methods (infrared, Raman and XRD) integrated with the density functional theory results, the heterostructures exhibited by CoS<sub>2</sub> and Cu<sub>2</sub>S could be regulated. The results show that the electron transfer/interaction between CoS<sub>2</sub> and Cu<sub>2</sub>S in the heterojunction were regulated, as well as the electronic structures of Co and Cu sites. As impacted by the structural engineering and the electronic modulation, the activity was enhanced, and the performance of electrocatalytic oxygen reactions was improved, which exhibited the lowest potential difference for ( $\Delta E = 0.73$  V) compared with commercial electrocatalysts. The liquid ZAB in accordance with on CoS<sub>2</sub>/Cu<sub>2</sub>S-NF exhibited a stable charge and discharge capacity up to 590 h and a great power density reaching 260.60 mW cm<sup>-2</sup>. Moreover, the flexible solid-state ZAB based on CoS<sub>2</sub>/Cu<sub>2</sub>S-NF exhibited a great competitive power density (92.06 mW cm<sup>-2</sup>), robust flexibility and an obvious integration. As compared with single metal sulfide-NF, the Density functional theory calculations (DFT) highlight the adsorption on CoS<sub>2</sub>/Cu<sub>2</sub>S-NF side surface in the heterojunction, which more specifically demonstrates the synergistic effect in the junction. This work presents a direction for designing heterostructured junctions as electrocatalyst and moreover its great application potential in rechargeable metal-solid batteries.

## 1. Introduction

As science and technology are developing rapidly, energy has been increasingly demanded by the modern society, while the sustainable development of environment and energy arouses rising attention. For broad technologies in terms energy storage and energy conversion, fuel cells and metal-air secondary battery act as the chemical power sources with a large capacity and a high energy ratio, thereby complying with the requirements of the next generation of green and sustainable energy technologies [1–3]. To be specific, the relevant flexible battery has been extensively valued for its light weight, flexibility and high safety. Besides, it is considered a promising power source with high prospect for in terms of portable wearable and portable wearable electronic devices, as

well as hybrid/electric vehicles [2,4]. The air electrode of the metal-air battery undergoes the slow kinetic ORR and OER when charging and discharging, thereby reducing energy efficiency and ultimately limiting the battery performance. Some precious metals (e.g., Ir, Ru and Pt-based catalysts) exhibiting a high OER activity are recognized as the optimal electrocatalytic oxygen reactant materials, whereas they are severely affected by the scarcity, high costs and the poor stability. As a result, their large-scale applications are restricted, and they achieve a low market penetration [5,6].

Transition metal-based [7–9] and non-metal-based electrocatalysts [10,11] (e.g., carbon materials) are characterized by their low costs, high activity and stability. The mentioned are recognized as the ideal substitutes for electrocatalytic oxygen reaction compounds. On the

\* Corresponding authors.

E-mail addresses: [liyili@szu.edu.cn](mailto:liyili@szu.edu.cn) (Y. Li), [renxz@szu.edu.cn](mailto:renxz@szu.edu.cn) (X. Ren).

<https://doi.org/10.1016/j.apcatb.2021.120849>

Received 30 June 2021; Received in revised form 6 October 2021; Accepted 24 October 2021

Available online 27 October 2021

0926-3373/© 2021 Elsevier B.V. All rights reserved.

whole, the existing electrocatalyst optimization methods refer to reducing the size to creating more active sites. Moreover, the effective electrochemical activity exhibited by the electrocatalyst refers to the combination with a 3D carbon or metal framework to enhance the electronic conductivity and the mass diffusion [12,13]. However, the methods of optimizing the mentioned methods fail to essentially regulate the intrinsic catalytic performance achieved by the active site. Accordingly, how to enhance the activity of the active site itself remains a vital topic in the catalytic reaction. The materials of the bimetallic heterojunction comprise: 1) abundant catalytic sites; 2) the regulation of the density of states at the Fermi level of the metal position to alter its inherent properties; 3) the modification of the catalytic Gibbs free energy [14–17]. Moreover, by employing the carbon materials exhibiting large specific surface areas as the conductive substrate, nano-alloy sizes and distributions are able to be effectively regulated. The electrocatalyst is capable of displaying a greater number of catalytic sites and an increased electrolyte/electrocatalyst contact area for facilitating the catalytic reactions. Over the past few years, oxygen [18] and Co [19] vacancies have been suggested to significantly enhance OER's catalytic activity via improved electronic structure, electron transfer capability and the charge density. Zhao et al. highlighted that oxygen vacancies are capable of increasing the electron mobility and the conductivity. Metal oxide electrocatalysts play an electrocatalytic role on the active center of oxygen reaction, while low-coordination metals can affect the catalytic performance exhibited by (001) crystal planes (e.g., Co-OOH) and do not satisfy the requirements [11]. Therefore, Nath et al. considered that with the introduction of copper exhibiting a high occupancy D band, the conductivity of the material could be enhanced, the charge transfer on the electrocatalyst surface could be improved, and the activity of the metal-based electrocatalyst could increase [14]. On the whole, copper-based electrocatalyst materials are prepared through the electrodeposition or the solid-state reaction, and the overpotential exhibited by most reported copper-based materials for the catalysis of OER basically ranges from 320 to 450 mV [7,20]. The formation of heterojunction can capable of altering the electron density of atoms around the interface [21]. In addition, non-metallic heteroatoms are capable of effectively modifying the surface structure of the transition metal-carbon materials, thereby regulating the electrocatalytic performance. For instance, S can generate more active sites and/or adjust the electronic configuration of the metal surface, thereby improving the results obtained by using oxygen reactions and rechargeable metal air [22–24]. Accordingly, the composition and electronic structures exhibited by active center was proved to be a means with high effectiveness for enhancing electrocatalytic activity.

Furthermore, the common powder electrocatalysts are limited in applications and the activity enhancement. First, when processing powdered materials onto the electrodes of the battery, a viscous polymer (e.g., Nafion, PTFE) should be introduced. Accordingly, the loss of catalytically active sites is caused during the processing, and internal particles turn out to be difficult to participate in the catalytic reaction. Second, during the catalysis, the powdered electrocatalyst is easily peeled off from the electrode substrate as impacted by the violent reaction or external forces. It is noteworthy that with the binders introduced, the high oxidation state of metal active sites can be destroyed in the electrode process, and the mentioned defects can be addressed with self-supporting electrodes [25]. The carbon substrate is capable of reducing the electrolyte-catalyst-electrode barrier, and the porous structures are capable of effectively increasing the number of active site and broadening the contact surface with the electrolyte [12,26]. Thus, the quality of catalytically active site, reactant adsorption and product desorption should be stressed in the catalysis to emphasize the novel combination of catalyst structures and components. However, such a type of material exhibits a complex structure, numerous elements and differences in the catalytic mechanism and the reaction kinetics of different materials, causing the key steps and control factors involved in the reaction to be controversial. The redox capabilities of various

electrocatalysts all show the differences, thereby causing different paths and mechanisms of redox reactions [27,28]. The mentioned will ultimately affect the power density, energy density, service life and efficiency of the ZAB. Thus, the corresponding in-situ technique in terms of characterization and the calculation of DFT are required for clarifying the reaction mechanism involved in the specific reaction of the catalyst, as well as guide the optimization of the structure and performance of the transition metal-carbon material.

In this study, a porous carbon material as a support was prepared by the electrospinning integrated with the high-temperature heat treatment. Besides, it was loaded with CoS<sub>2</sub>/Cu<sub>2</sub>S heterojunction metal particles and acted as bifunctional electrocatalyst exhibiting great efficiency for oxygen reactions. the CoS<sub>2</sub>/Cu<sub>2</sub>S heterojunction was the main active site, which significantly improved the electrochemical performance. In addition, the porous carbon fiber achieved an excellent flexibility, whereas it also contributed to the charge transport in ORR/OER. As impacted by the highly efficient active sites, structure and mechanical properties, the optimized CoS<sub>2</sub>/Cu<sub>2</sub>S-NF could achieve an excellent dual-functional catalysis. In the half-cell test, CoS<sub>2</sub>/Cu<sub>2</sub>S-NF showed the lowest potential gap ( $\Delta E = 0.73$  V). The liquid electrolyte-based ZAB employing CoS<sub>2</sub>/Cu<sub>2</sub>S-NF as a catalyst showed a great particular capacity up to 812.78 mA h g<sup>-1</sup>, energy density to 260.60 Wh kg<sup>-1</sup>, as well as a long work time of 590 h under 5 mA cm<sup>-2</sup>. Furthermore, the flexible rechargeable ZAB with the use of self-supporting CoS<sub>2</sub>/Cu<sub>2</sub>S-NF to be the air cathode showed a great energy density (92.06 mW cm<sup>-2</sup>), prominent cycle (23 h at 5 mA cm<sup>-2</sup>) as well as flexibility. An in-depth research was conducted on the electrocatalytic reaction mechanism of the material in the battery. The adsorption and desorption process of CoS<sub>2</sub>/Cu<sub>2</sub>S on different active intermediate species, the effect of heterojunction and the adsorption and desorption of various active intermediate species are were demonstrated by DFT calculation and in-situ characterization technology. The influence onto the stability and electrocatalytic activity by the electrocatalyst could theoretically and technically support the industrialization of rechargeable ZAB.

## 2. Experimental

### 2.1. Materials

Iridium carbon (Ir/C, 99.9%), copper nitrate (Cu(NO<sub>3</sub>)<sub>2</sub>•6H<sub>2</sub>O, AR), polyacrylonitrile (PAN, AR), cobalt nitrate hexahydrate (Co(NO<sub>3</sub>)<sub>2</sub>•6H<sub>2</sub>O, AR), platinum carbon (20 wt% Pt/C), sulfur powder (S, AR), potassium hydroxide (KOH, AR), ethanol (CH<sub>3</sub>CH<sub>2</sub>OH, chemically pure, 95%), zinc acetate (Zn(Ac)<sub>2</sub>, AR) were provided by Aladdin. Polyvinyl alcohol (PVA) originated alfa, Polyethylene-polypropylene glycol (F127, Mn ~ 13000) offered by Macklin. All chemicals and materials were used without being further purified. On the whole, ethanol (chemically pure, 95%), zinc foil, foamed nickel aluminum foil, potassium hydroxide and zinc acetate were purchased from Guangzhou Chemical Reagent Factory.

### 2.2. Synthesis of CoS<sub>2</sub>/Cu<sub>2</sub>S-NF

The addition of 1 g PAN, 513.5 mg Co(NO<sub>3</sub>)<sub>2</sub>•6H<sub>2</sub>O and 460 mg F127 was achieved in 10 mL N,N-Dimethylformamide (DMF). The stirring of the resulting solution was achieved quickly at ambient temperature for 12 h, They were mixed well till the solution was evenly mixed, and no obvious bubbles were found.

The electrospinning device applied here covered a collector (stainless steel plate), a grounding electrode, a high-voltage power supply and a syringe and needle ( $\Phi = 0.84$  mm). The flow rate was controlled by the syringe pump linked with the syringe. The PAN-based nanofiber membranes were formed by the electrospinning under 0.75 mL h<sup>-1</sup> solution flow rate, a distance of 15 cm to the collector from the tip of the needle, 1 kV negative voltage, as well as 15 kV positive voltage. The experimental process was performed at 25 °C and under 60% ambient

humidity. PAN-based nanofiber membrane was peeled from the aluminum foil. Subsequently, an oven was used to dry membrane at 60 °C for 6 h. The dried PAN-based nanofiber membrane was heat-treated. First, it was pre-oxidized within a tube furnace within the air atmosphere. This study regulated the temperature as 280 °C, the heating rate was 1 °C min<sup>-1</sup>, and the temperature was kept for 1 h to obtain pre-oxidized PAN-based nanofiber membrane.

200 mg of PAN-based nanofiber membrane and 1000 mg of sulfur powder were weighed and spread in two porcelain boats, respectively. The porcelain boat containing sulfur powder was placed at one end close to the tube furnace's air inlet, and the porcelain boat containing the pre-oxidized PAN-based nanofiber membrane was arranged at the end close to the tube furnace's air outlet. In the N<sub>2</sub> atmosphere, the temperature rose from ambient temperature to 280 °C at 2 °C min<sup>-1</sup>, and this study maintained the temperature for 1 h. Then, the heating of boats was achieved at 5 °C min<sup>-1</sup> to 800 °C, and this study maintained the temperature for 2 h. Furthermore, sulfur-doped carbon nanofibers were generated.

### 2.3. Synthesis of control samples

In comparison, the reaction conditions remained unchanged, and the samples obtained by altering the raw material (Cu<sup>2+</sup>:Co<sup>2+</sup>) and introducing the molar ratio (5:0, 0:5, 5:5) were termed as Cu<sub>2</sub>S-NF, CoS<sub>2</sub>-NF, CoS<sub>2</sub>/Cu<sub>2</sub>S-NF, respectively. To be specific, NF indicates that no metal source was added to the electrospinning dope with the above reaction conditions unchanged.

### 2.4. Characterization

Zeiss company's JEM-2100F transmission electron microscope (TEM) and Merlin field emission scanning electron microscope (FE-SEM) were employed for characterizing the microscopic morphologies and the internal structures, respectively. The element content and the elements' valence state on the sample surface were measured by applying the X-ray photoelectron spectrometer (XPS) with Al K $\alpha$  rays (1486.6 eV). With a multiple-functional powder X-ray diffractometer (XRD, XPert Powder), the characterization was conducted for the crystal structure and phase of the catalyst. This study employed the Raman (LabRAM Aramis of H.J.Y, France) for primarily characterizing defects of the catalyst. The instrument applied in the test of attenuated total reflection of the Fourier infrared spectroscopy was the Nicolet 6700 Fourier transform infrared spectrometer, which was a qualitative analysis of the intermediates on the sample surface in the electrochemical reaction. The thermogravimetric analysis was conducted by adopting the STA499 thermogravimetric analyzer of Germany NETZSCH company. When the carbon deposition analysis was being conducted, in an air (30 mL min<sup>-1</sup>), the heating rate reached 10 °C min<sup>-1</sup>, and the sample load reached 5–10 mg.

To perform the half-cell experiment of the electrochemical test, the conventional three-electrode system was adopted, and the rotating disk electrode (Autolab) and electrochemical workstation (CHI 760E) were employed in 1 M KOH electrolyte solution. The carbon rod was the counter electrode, the Ag/AgCl electrode acted as the electrode to be referenced, and the glassy carbon electrode was the working electrode (GCE, diameter 4 mm). 5 mg of the electrocatalyst was weighed and ground evenly. Then, it displayed an ultrasonic dispersion in 1.5 mL of a mixed solution containing ethanol and Nafion (V/V=1500:20). A pipette was used to take 10  $\mu$ L of the dispersion liquid drop on glassy carbon electrode surface. Next, the liquid drop was placed on the glassy carbon electrode surface and then dried at ambient temperatures. The linear sweep test (LSV) sweep speed reached 5 mV s<sup>-1</sup>. The potential in the article was overall changed to a relatively reversible hydrogen electrode (RHE) by:  $E(\text{RHE}) = E(\text{Ag/AgCl}) + 0.059 \text{ pH} + 0.197$  [11].

The liquid ZAB employed zinc flakes as the negative electrode, adopted an air catalyst coated on carbon fiber paper to be positive electrode, and applied 6.0 M KOH as the electrolyte. For ensuring that

the redox reaction on the zinc anode could be performed in a reversible manner, the dissolution of 0.2 M Zn(Ac)<sub>2</sub> was achieved within the electrolyte. 5 mg of the sample was weighed and introduced into 1 mL of distilled water/ethanol solution at 4:1 vol ratio. The mechanical mixture of commercial Pt/C and Ir/C (mass ratio = 1:1) was treated as the control group. Subsequently, the resulting slurry was mixed with 140  $\mu$ L of Nafion solution, applied on the carbon paper, and dried at 60 °C. A positive electrode with a load of nearly 5.0 mg cm<sup>-2</sup> was obtained. For the solid-state ZAB after 12 h, polished zinc foil (0.01 mm thick) acted as the anode. The preparing process of gel polymer electrolyte included: based on the magnetic stirring for 2 h at 95 °C, the dissolution of PVA (1.0 g) was achieved in deionized water (10 mL). Subsequently, 1.0 mL of 18.0 M KOH containing 0.02 M Zn(Ac)<sub>2</sub> was introduced, and the stirring process of the electrolyte was conducted at 95 °C for 40 min. Afterwards, the freezing process of the solution was achieved under the temperature of -20 °C for 20 h, and then the thawing process of under the ambient temperatures. This study carried out the mentioned process two times to gel the PVA. Next, a solid-state ZAB was assembled by placing a lignin-derived hollow carbon nanofiber membrane and a zinc foil on both sides of the PVA gel, respectively. Moreover, a piece of pressed Ni foam acted as the current collector on the air electrolyte side.

This study determined the cycle performance and discharge/charge performance exhibited by the ZAB with the LAND-CT2001A test device. The current density of the cycle performance test was 5 mA cm<sup>-2</sup>, the cycle test period of the water-based ZAB was 1200 s. In addition, the cycle test period of the flexible ZAB was 2400 s. The polarization curve was tested on the electrochemical workstation.

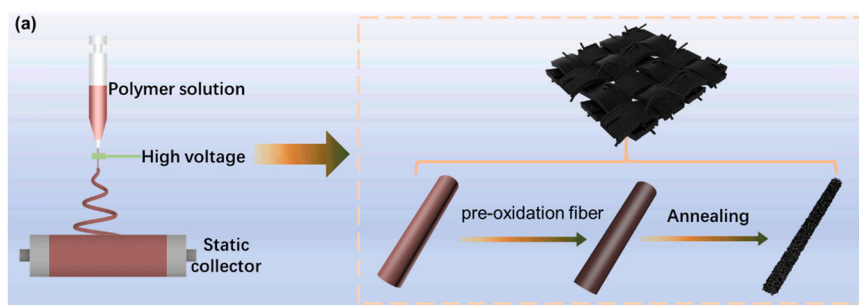
**In-situ characterization test:** By using the X-ray powder diffractometer (D8 ADVANCE, Bruker AXS GmbH Co., Ltd), this study recorded in-situ XRD measurement. This study determined in-situ Raman spectra with the HR800 Raman spectrometer (HORIBA JobinYvon), and the in-situ FTIR spectra were tested by using the Nicolet 6700. Next, the flexible ZAB equipped with CoS<sub>2</sub>/Cu<sub>2</sub>S-NF as the electrocatalyst was subjected to the relevant in-situ test and characterization in the charge and discharge tests. To be specific, the in-situ infrared and in-situ Raman were used. When the experimental data were being collected, the current density of the cycle performance test was 5 mA cm<sup>-2</sup>, and the period was 1200 s. When the experimental data were being collected by using the in-situ XRD, the battery cycle performance test parameters were 0.5 mA cm<sup>-2</sup> current density and 1200 s as a cycle.

## 3. Results and discussion

### 3.1. Material structure characterizations

The preparation of CoS<sub>2</sub>/Cu<sub>2</sub>S-NF is illustrated in Scheme 1. PAN was prepared into a fiber film by the electrospinning. Subsequently, it underwent the pre-oxidation, the sulfur doping and the high-temperature annealing treatment. Lastly, CoS<sub>2</sub>/Cu<sub>2</sub>S-NF was obtained. Fig. 1a presents a digital photo of CoS<sub>2</sub>/Cu<sub>2</sub>S-NF. The material could be bent at a range of angles (up to 180°) and be restored to a straight state, which demonstrated that the material exhibited a high flexibility, thereby making it a self-supporting electrode. The electrodes were likely to effectively avoid the use of inactive binders, ensure the stable adhesion of the catalyst under wide operating voltages, and achieve the improved battery performance. The morphology and structure of the material could be a vital factor affecting the catalytic activity of the material. The SEM image of CoS<sub>2</sub>/Cu<sub>2</sub>S-NF is illustrated in Fig. 1b. The diameter of the carbon fiber tube was approximately 500 nm. There were numerous pores and metal particles in the sample. In comparison, the sample without any particles displayed a smoother surface (Fig. S1), whereas the porous structure could be identified from the cross section of the tube. When the sample contains only a single metal sulfide, the surface roughness and porosity of carbon nanofibers are significantly reduced (Fig. S2-S3). This porous structure broadened the active surface of the electrocatalyst, which could improve the electrocatalytic oxygen





**Scheme 1.** Diagram of the preparation process for CoS<sub>2</sub>/Cu<sub>2</sub>S-NF.

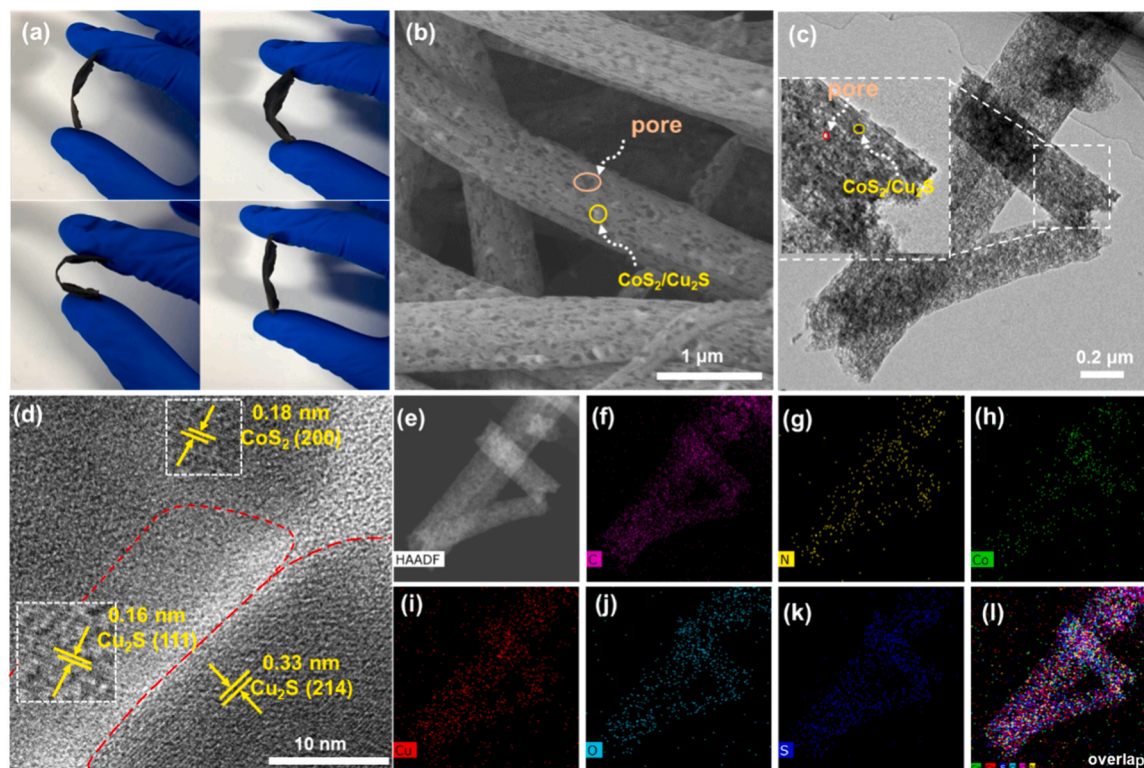


**Fig. 1.** (a) Photographs of CoS<sub>2</sub>/Cu<sub>2</sub>S-NF films under flattening, bending and recover states; (b) SEM; (c) TEM and (d) high magnifications of HRTEM image; (e) HAADF-STEM images and the corresponding elemental mappings of (f) C, (g) N, (h) Co, (i) Cu, (j) O, (k) S and (l) overlap of CoS<sub>2</sub>/Cu<sub>2</sub>S-NF.

reaction activity of the material [29]. As obviously indicated from the TEM image, the carbon fiber was filled with the dense pores and evenly filled with small particles (Fig. 1c). As indicated from the in-depth qualitative analysis of CoS<sub>2</sub>/Cu<sub>2</sub>S-NF by using the HRTEM, the lattice spacing was 0.16 nm, resulting from the (200) crystal plane of CoS<sub>2</sub>. The (111) and (120) crystal planes were largely exposed to Cu<sub>2</sub>S (Fig. 1d). As shown in Fig. S8, Selected area electron diffraction image of CoS<sub>2</sub>/Cu<sub>2</sub>S-NF shows several rings that show the (222), (220), (211) and (200) planes of CoS<sub>2</sub> and the (111), (214) and (201) planes of Cu<sub>2</sub>S, corresponding to the result of XRD and HRTEM. As clearly indicated from the high-angle circular dark field (HAADF-STEM) image (Fig. 1e), the CoS<sub>2</sub>/Cu<sub>2</sub>S-NF comprised two parts, i.e., the dark part and the bright part that were evenly distributed on the porous carbon fiber. According to the mapping image of the elements, most of the bright spots of C, N, O, S, Cu and Co elements had even distributions, which demonstrated that the metals and heteroatoms were evenly distributed on the porous carbon fiber. (Fig. 1f-l).

As indicated from the XRD pattern in Fig. 2a, with the standard cards of CoS<sub>2</sub> (PDF #89-3056) and Cu<sub>2</sub>S (PDF #72-1071), and the 2θ values are 27.96°, 32.39°, 39.95°, 46.47° and 55.11°, corresponding to CoS<sub>2</sub>

(111), (200), (211), (220) and (311) crystal planes [30], respectively. The characteristic peaks at 2θ values of 27.32°, 32.64°, 35.50°, 46.10° and 53.76° corresponded to Cu<sub>2</sub>S (102), (111), (112), (201) and (212), respectively [31]. Moreover, NF only exhibited (002) and (101) characteristic peaks of graphite corresponding to 26° and 43° [1]. As verified from the results, it was largely presented CoS<sub>2</sub> and Cu<sub>2</sub>S in the composite.

In the Raman spectrum of different samples in Fig. 2b, there were two significant peaks at the wavenumbers of 1565.69 and 1339.4 cm<sup>-1</sup>, in correspondence to and the graphitized carbon (G band) and the disordered carbon (D band), acted as a vital parameter to judging the sample defects. The I<sub>D</sub>/I<sub>G</sub> value of CoS<sub>2</sub>/Cu<sub>2</sub>S-NF equaled 1.02, which was slightly higher than that of NF (0.93), which demonstrated that the defect degree of carbon materials could be effectively elevated with the metal sulfide. The mentioned feature helped improve the electrocatalytic oxygen reaction performance of the material [32]. The data of the metal content in the sample was collected by a thermogravimetric analyzer in an air atmosphere (Fig. 2c). When the temperature increased from ambient temperature to 120 °C, the weight loss occurring was the sample's loss of water. The final residual amounts of samples NF,



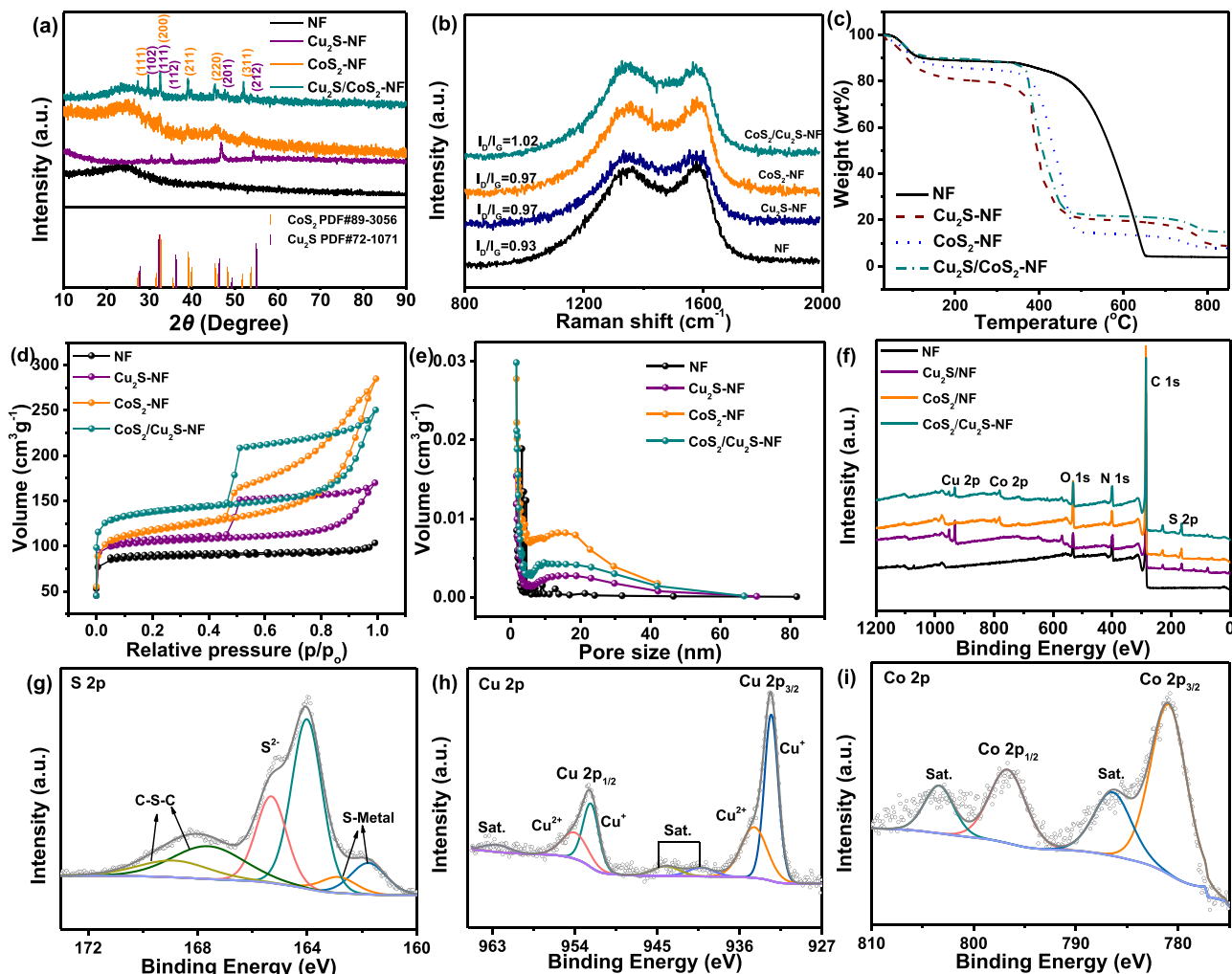


Fig. 2. (a) XRD pattern, (b) Raman spectra, (c) TGA curves, (d) nitrogen adsorption-desorption isotherms and (e) pore-size curves of samples; XPS survey spectra of (f) samples, and high-resolution (g) S 2p, (h) Co 2p and (i) Cu 2p XPS spectra of CoS<sub>2</sub>/Cu<sub>2</sub>S-NF.

Cu<sub>2</sub>S-NF, CoS<sub>2</sub>-NF and CoS<sub>2</sub>/Cu<sub>2</sub>S-NF were 0%, 9.67 wt%, 9.66 wt%, and 20.74 wt%, respectively. The two weight loss of the sample containing metal sulfides between 400 °C and 850 °C primarily resulted from the decomposition of the carbon material in the sample and the conversion of the sulfide metal to oxide in an oxygen atmosphere [33].

The specific surface area exhibited by the electrocatalyst was quantitatively investigated by performing the BET test. Fig. 2d presents the type IV isotherm with H3-type hysteresis in terms of the sample. At a relative high-pressure ratio ( $P/P_0$ ), all samples except for NF achieved the obvious hysteresis loops, which demonstrated the coexistence of the micropores and the mesopores in the samples. The calculated specific surface areas of CoS<sub>2</sub>-NF, Cu<sub>2</sub>S-NF, CoS<sub>2</sub>/Cu<sub>2</sub>S-NF and NF are 6.1, 138.3, 379.7 and 404.6 m<sup>2</sup> g<sup>-1</sup>, respectively. As indicated from the results, the specific surface area of the sample was expanded with the introduction of metal sulfides to the material. Moreover, the pore size distribution of the sample is presented in Fig. 2e. As indicated from the mentioned characterization, CoS<sub>2</sub>/Cu<sub>2</sub>S-NF displayed a porous structure and a greater BET surface area, which contributed to the mass transfer in the electrochemical oxygen reactions [3].

To characterize the surface element composition of the sample and the chemistry state of the respective element, the XPS test and the result analysis on the sample were performed. Fig. 2f presents the XPS survey spectrum of different samples, with the characteristic peaks of Co, Cu, O, N, S and C of CoS<sub>2</sub>/Cu<sub>2</sub>S-NF and the content of the mentioned elements: 1.26 at%, 0.79 at%, 6.79 at%, 9.88 at%, 2.68 at% and 78.59 at%. The

high resolution spectra of S 2p of CoS<sub>2</sub>-NF, Cu<sub>2</sub>S-NF and CoS<sub>2</sub>/Cu<sub>2</sub>S-NF samples are showed in Fig. 2g, Fig. S4b and Fig. S5b. As impacted by the different types of sulfur in the samples, they exhibited the similar multiple peaks. Through the Gaussian fitting, the peaks of the high-resolution XPS spectrum of S 2p at 161.7 and 162.8 eV represents the typical metal sulfur bond, respectively [2]. The deconvolution peaks at 164.2 eV and 165.4 eV were an indicator of the presence of S<sup>2-</sup> in a low coordination state on the surface [34]. The deconvolution peaks at 167.5 eV and 169.0 eV were the characteristic peak of thiophene-S (C-S-C) [35]. During the vulcanization, a part of S atoms doped into NF positively impacted on the ORR/OER activity [2,36]. The Cu 2p peaks were divided (Fig. 2h and Fig. S4a) into seven peaks. There were two characteristic peaks of Cu<sup>1+</sup> at 932.7 and 952.6 eV, respectively. Furthermore, the satellite peaks of Cu<sup>1+</sup> were located at 944.5 eV. The double peaks at (934.9 and 954.9 eV) and (940.9 and 962.6 eV) represented to the characteristic peak of Cu<sup>2+</sup> and its satellite peaks, respectively [37]. Fig. 2i and Fig. S5a illustrate the high-resolution Co 2p XPS spectrum of CoS<sub>2</sub>/Cu<sub>2</sub>S-NF, in which the binding energy of Co 2p high-resolution spectrum was located at (780.9 and 796.8 eV), representing the characteristic peaks of Co 2p<sub>3/2</sub> and Co 2p<sub>1/2</sub>, respectively. As indicated from the fitting curves of Co 2p<sub>3/2</sub> and Co 2p<sub>1/2</sub>, Co<sup>2+</sup> coexisted in CoS<sub>2</sub>/Cu<sub>2</sub>S-NF. Furthermore, the satellite peaks of Co<sup>2+</sup> were located at 786.5 and 803.4 eV [2,38].

### 3.2. Electrochemical activity and mechanism

To assess the electrocatalytic ORR performance of the samples, several electrochemical tests were carried out on the prepared samples and the commercial precious metal materials. Fig. 3a plots the LSV curve of ORR catalyzed by different electrocatalysts. As indicated from the results, CoS<sub>2</sub>/Cu<sub>2</sub>S-NF shows the superior ORR activity. The half-wave potential value ( $E_{1/2}$ ) of CoS<sub>2</sub>/Cu<sub>2</sub>S-NF (0.80 V) and Pt/C (0.83 V) was comparable, which was significantly higher than those of Cu<sub>2</sub>S-NF (0.67 V), CoS<sub>2</sub>-NF (0.73 V) and NF (0.72 V). Furthermore, the Tafel value of the samples was obtained according to the LSV in Fig. 3a to clarify the ORR electrocatalytic kinetic performance of the sample (Fig. 3b). Compared with other samples, the Tafel slope value of CoS<sub>2</sub>/Cu<sub>2</sub>S-NF was only 88.06 mV dec<sup>-1</sup>, which was better than Cu<sub>2</sub>S-NF (191.04 mV dec<sup>-1</sup>), NF (276.58 mV dec<sup>-1</sup>) and Pt/C (98.27 mV dec<sup>-1</sup>). As indicated from the mentioned data, CoS<sub>2</sub>/Cu<sub>2</sub>S-NF, a catalyst with the excellent ORR activity, could effectively reduce the overpotential of ORR.

By employing RRDE to measure the hydrogen peroxide yield and the number of electron transfers during the catalyzed ORR process of the sample, the reaction mechanism of the sample catalyzed ORR could be elucidated. According to Fig. 3c, in the potential range of 1.00–0.23 V, CoS<sub>2</sub>/Cu<sub>2</sub>S-NF exhibited the maximal  $n$  value of nearly 3.74 and the

lowest hydrogen peroxide yield of about 11.21%, which was comparable to those of Pt/C (3.76; 12.20%). As confirmed from the similar characteristics, the ORR reaction mechanism catalyzed by CoS<sub>2</sub>/Cu<sub>2</sub>S-NF could be a 4-electron reaction pathway. Overall, CoS<sub>2</sub>/Cu<sub>2</sub>S-NF exhibited an excellent catalytic activity similar to that of commercial Pt/C electrocatalysts, and it even exceeded Pt/C electrocatalysts in terms of reaction kinetics. The stability of the electrocatalyst could also act as a major indicator of the application. The experiment generally employed the chronoamperometry to evaluate the durability and anti-poisoning of the catalyst. In addition, by adding 1 M methanol to the alkaline solution saturated with O<sub>2</sub>, the anti-toxicity of the material could be effectively monitored. According to Fig. 3d, CoS<sub>2</sub>/Cu<sub>2</sub>S-NF was almost completely unaffected by methanol. On the contrary, Pt/C is very sensitive to methanol. As shown in Fig. 3e, after the stability test was performed, the current density corresponding to the commercial Pt/C half-wave potential was only 53.49% of the initial current density (38.75 h). However, the limiting current density of CoS<sub>2</sub>/Cu<sub>2</sub>S-NF was 70.67% of the initial current density (40 h), thereby suggesting that CoS<sub>2</sub>/Cu<sub>2</sub>S-NF exhibited better stability. The OER performance of the samples was first characterized under with a standard three-electrode system. As indicated from the linear scan curve in Fig. 3f, the overpotential value of the sample CoS<sub>2</sub>/Cu<sub>2</sub>S-NF at 10 mA cm<sup>-2</sup> was 348 mV, which is better than those of Cu<sub>2</sub>S-NF (443 mV), CoS<sub>2</sub>-NF (347 mV), and comparable to Ir/C

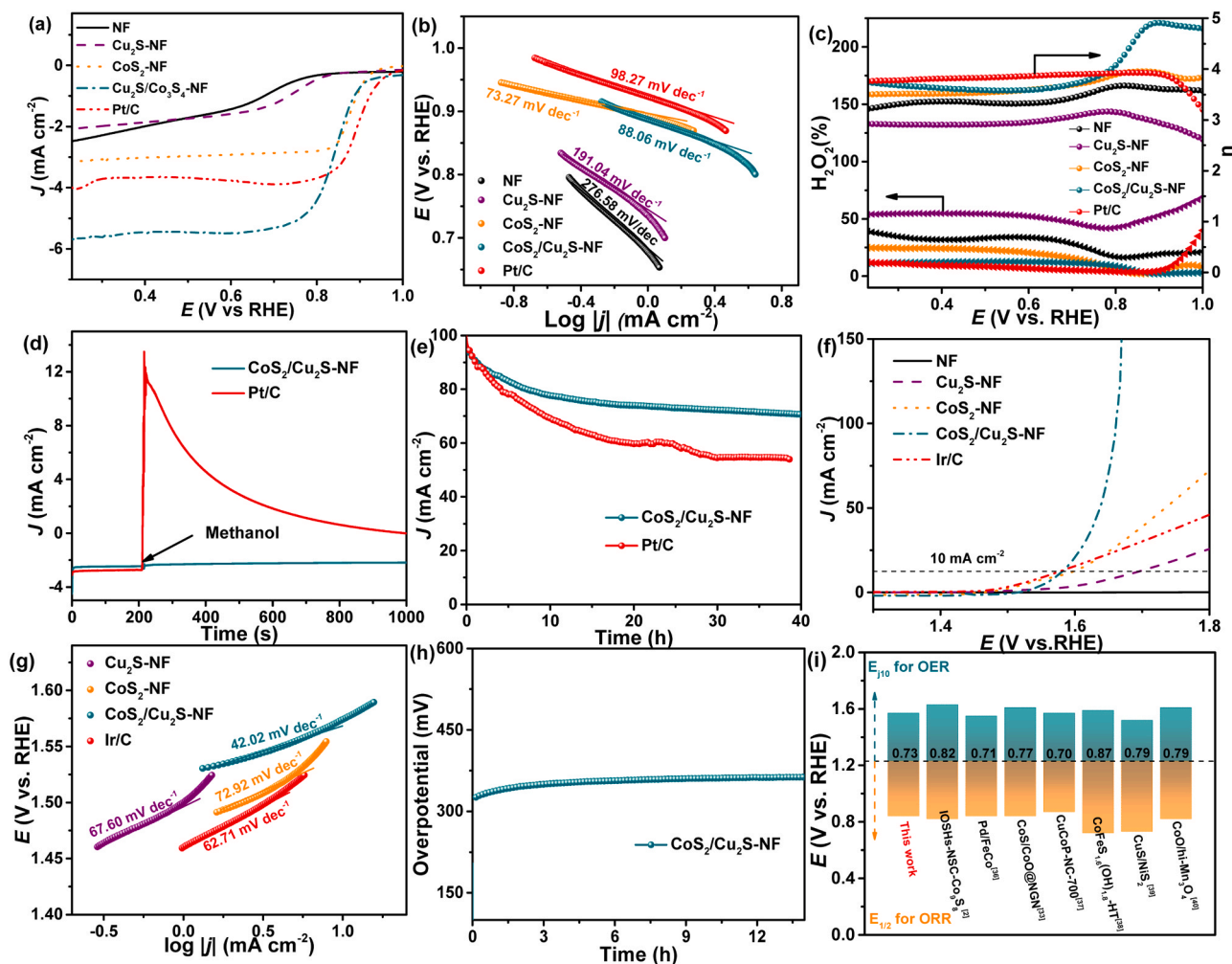


Fig. 3. ORR performances of the as-prepared catalysts in alkaline medium: (a) linear sweep voltammograms (LSVs) on different catalysts in O<sub>2</sub>-saturated 1.0 M KOH with a scan rate of 5 mV s<sup>-1</sup> and a rotation speed of 1600 rpm, (b) Tafel plots; (c) the peroxide yield and electron transfer number of different catalysts; (d) Current time chronoamperometric response of ORR at CoS<sub>2</sub>/CS-800 and Pt/C electrodes for methanol crossover tolerance test and (e) durability evaluation; (f) IR-corrected LSV curves of OER in 1.0 M KOH at 1600 rpm, and (g) Tafel plots; (h) Chronopotentiometry curve of OER at 10 mA cm<sup>-2</sup> for durability evaluation; (i) Comparison of bifunctional performance between  $E_{1/2}$  for ORR and  $E_{j=10}$  for OER on various catalysts.

(329 mV). In addition, the Tafel value of the sample was derived from the LSV in Fig. 3g to clarify the OER kinetic performance of the sample. The Tafel slope of CoS<sub>2</sub>/Cu<sub>2</sub>S-NF (42.02 mV dec<sup>-1</sup>) was lower than those of CoS<sub>2</sub>-NF (72.92 mV dec<sup>-1</sup>), Cu<sub>2</sub>S-NF (67.60 mV dec<sup>-1</sup>), and Ir/C (62.71 mV dec<sup>-1</sup>). It was therefore suggested that CoS<sub>2</sub>/Cu<sub>2</sub>S-NF exhibited the optimal intrinsic kinetic activity. Furthermore, as demonstrated by using the constant potential test method, the potential value of CoS<sub>2</sub>/Cu<sub>2</sub>S-NF remained changed insignificantly after 14 h of testing (Fig. 3h).

The reversible potential difference ( $\Delta E$ ) of the electrocatalytic ORR/OER reaction, refers to the potential value ( $E_{10}$ ) corresponding to the current density of the OER LSV curve under the current density of 10 mA cm<sup>-2</sup> minus the half-wave potential value of the ORR LSV curve ( $E_{1/2}$ ), which could act as a vital parameter to evaluate the application of bifunction electrocatalysts to metal-air batteries as air cathode catalysts. The  $\Delta E$  value of CoS<sub>2</sub>/Cu<sub>2</sub>S-NF is 0.73 V (Fig. 3i). It was therefore indicated that the CoS<sub>2</sub>/Cu<sub>2</sub>S-NF electrocatalyst prepared in this study could exhibit an excellent electrochemical activity and a bifunctional reversibility, and it could show wide application prospects in metal-air batteries. According to the bifunctional ORR/OER activity of CoS<sub>2</sub>/Cu<sub>2</sub>S-NF in most of the existing studies, the reported benchmark

bifunctional electrocatalyst was at a relatively high level [2,36,39–43], which further proved the basic principle of CoS<sub>2</sub>/Cu<sub>2</sub>S-NF as a bifunctional electrocatalyst for high-performance ZAB. The high performance obtained was attributed to the following advantages exhibited by the favorable composition and structure of CoS<sub>2</sub>/Cu<sub>2</sub>S-NF. First, carbon nanofibers could act as a carrier for stabilizing CoS<sub>2</sub>/Cu<sub>2</sub>S, and they could form small-sized CoS<sub>2</sub>/Cu<sub>2</sub>S hetero-bonded gold via the nano-scale restriction, in which CoS<sub>2</sub>/Cu<sub>2</sub>S was used as the catalytic material for ORR and OER, respectively. Second, the doping of sulfur would alter the electronic performance of the electrocatalyst and promote the electron transfer of the reaction. Accordingly, it could be beneficial to increase the availability of active species on the porous fibrous material of the CoS<sub>2</sub>/Cu<sub>2</sub>S matrix. The mentioned inherent advantages were previously demonstrated in metal-based materials, carbon fiber materials and heteroatom-modified metal materials [22,37,44, 45].

To investigate the catalytic performance of CoS<sub>2</sub>/Cu<sub>2</sub>S-NF as electrocatalyst in the actual operation of the battery, a ZAB with Zn sheet was employed as the negative electrode, and that with carbon sheet was adopted as the air positive electrode. For comparison, a ZAB with Pt/C+Ir/C as the battery catalyst was tested under the identical conditions.

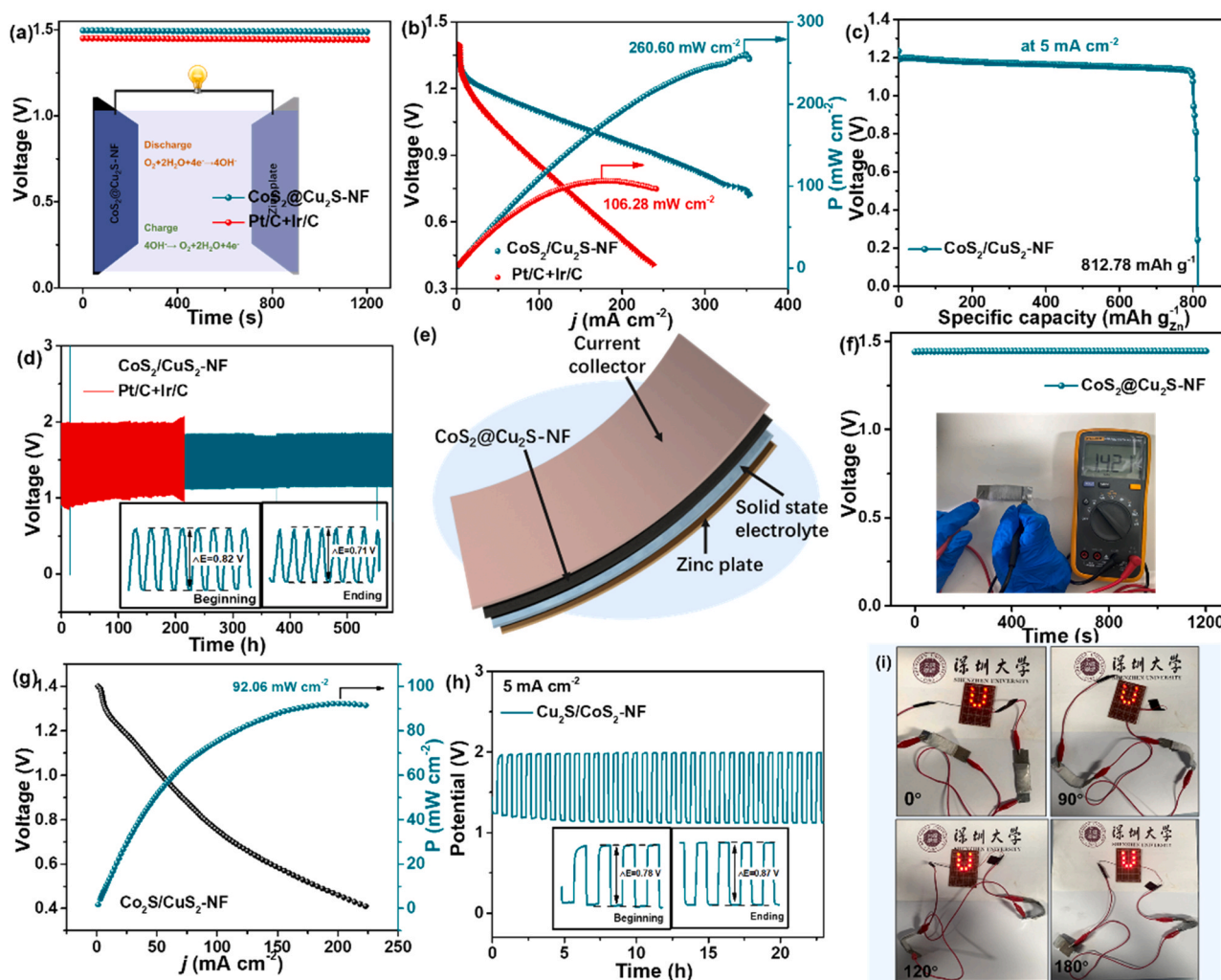


**Fig. 4.** (a) Open-circuit plots of liquid ZABs (inset: Schematic of the liquid ZAB); (b) discharge polarization curves and the corresponding power density; (c) Specific capacity plots and (d) Galvanostatic discharge-charge cycling curves at 5.0 mA cm<sup>-2</sup> of the liquid ZABs (inset: Enlarged cycle voltage profiles of ZAB with the CoS<sub>2</sub>/Cu<sub>2</sub>S-NF cathode); (e) Schematic of the wearable ZAB. (f) Open-circuit plots of wearable ZAB (inset: Photograph of CoS<sub>2</sub>/Cu<sub>2</sub>S-NF-based wearable ZAB displaying measured open-circuit voltage). (g) discharge polarization curves and corresponding power density; (h) Galvanostatic discharge-charge cycling curves at 5 mA cm<sup>-2</sup> (inset: Enlarged cycle voltage profiles of ZAB with the CoS<sub>2</sub>/Cu<sub>2</sub>S-NF cathode); (i) Photographs of 8 red LED lightened by two flexible ZABs connected in series when bended at various angles.



According to Fig. 4a, the liquid ZAB achieved a high open circuit voltage of 1.49 V, and the open circuit of Pt/C+Ir/C was 1.44 V and remained stable in 1200 s. The charge and discharge polarization curves of the ZAB are shown in Fig. S5a. CoS<sub>2</sub>/Cu<sub>2</sub>S-NF as the positive electrocatalyst for battery exhibited a current density similar to that of Pt/C+Ir/C. According to Fig. 4b, during the discharge, the liquid ZAB made of CoS<sub>2</sub>/Cu<sub>2</sub>S-NF as the cathode catalyst was suggested to exhibit current density of (170.4 mA cm<sup>-2</sup>, 1.0 V), which was significantly higher than Pt/C+Ir/C (58.92 mW cm<sup>-2</sup>, 1.0 V). The power density of CoS<sub>2</sub>/Cu<sub>2</sub>S-NF was 260.60 mW cm<sup>-2</sup> at 0.56 V, and the current density was 255.47 mA cm<sup>-2</sup>, which was significantly better than that of Pt/C (105.70 mW cm<sup>-2</sup>, 0.73 V, 145.01 mA cm<sup>-2</sup>), and exceeded lots of metal-air battery reported recently (Table S1). As suggested from the discharge curve of CoS<sub>2</sub>/Cu<sub>2</sub>S-NF ZAB, the specific capacity under a current density of 5 mA cm<sup>-2</sup> was 812.78 mAh g<sup>-1</sup> (based on the mass of Zn), and the corresponding energy density reached up to 975.34 Wh kg<sup>-1</sup> (Fig. 4c). Fig. 4d illustrates the cycle curve durability test of a liquid ZAB under a current density 5 mA cm<sup>-2</sup> and a cycle period of 1200 s, which revealed that the initial charge and discharge potential of a liquid ZAB based on CoS<sub>2</sub>/Cu<sub>2</sub>S-NF. The initial voltage gap was only 0.71 V, and the charge-discharge potential difference after 580 h (1740 cycles) was 0.82 V, and no obvious voltage attenuation was identified. The battery employing Pt/C+Ir/C as the electrocatalyst indicated a significant voltage drop after 215 h (645 cycles). As shown in Fig. S10, XPS of CoS<sub>2</sub>/Cu<sub>2</sub>S-NF after the cyclic stability test. The existence of Co, Cu, O, N, S and C in the CoS<sub>2</sub>/Cu<sub>2</sub>S-NF were 0.76 at%, 0.94 at%, 15.04 at%, 2.89 at%, 3.81 at% and 76.56 at%, respectively. The CoS<sub>2</sub>/Cu<sub>2</sub>S-NF catalyst still maintained its porous fibre morphology after the charge/discharge cycling test, as confirmed by TEM (Fig. S9). However, compared with fresh prepared samples, the characteristic peaks of S-O at 171.3 and 172.7 eV were appeared [36], implying some part of the non-metal sulfur counterparts of the metal sulfide was oxidized into sulfate and dissolved in the electrolyte or adsorbed on the surface of the catalyst (Fig. S10b). The adsorption of sulfate on the surface can mediate water oxidation and accelerate the oxygen evolution reaction process through proton-coupled electron transfer [46–48]. In addition, the binding energy of Co 2p<sub>3/2</sub> is at 783.9 eV, which is higher than the as-prepared sample, indicating that the higher oxidation state of the sulfide is converted to high oxidation state cobalt (Fig. S10d). The high oxidation state of cobalt can facilitate the O\* adsorption and promote the OER catalytic activity of cobalt sulfide [49]. As shown in Fig. S10c, the XPS peak of Cu<sup>2+</sup> is stronger than before because part of the Cu<sub>2</sub>S exposed on the surface of the carbon fiber is partially oxidized during ZAB running [50]. According to the in-situ characterization methods and the TEM and XPS results after the discharge/charge test, it can be seen that the original morphology and structure of the sample are maintained, while there is a certain degree of oxidation on the surface of the metal sulfides. However, the as-prepared CoS<sub>2</sub>/Cu<sub>2</sub>S-NF composite can still achieve the excellent electrochemical performance which can reveal that the combination of metal sulfide and carbon material may effectively improve the conductivity and stability of the material, and expose more active sites, which are the main reasons for the improvement of the catalytic activity and excellent stability of the composite material [51]. As revealed from the mentioned results, the liquid ZAB by using CoS<sub>2</sub>/Cu<sub>2</sub>S-NF as the positive electrode electrocatalyst exhibited a prominent cycle stability. The mentioned results confirmed that CoS<sub>2</sub>/Cu<sub>2</sub>S-NF could act as an efficient and stable catalyst for the rechargeable ZABs (Table S1).

To investigate its application in wearable electronic products, self-supporting CoS<sub>2</sub>/Cu<sub>2</sub>S-NF fiber membrane acted as the air cathode, alkaline polyvinyl alcohol gel was used as the electrolyte, flexible zinc foil was employed as the anode, and nickel foam was used as the current collector to assemble rechargeable flexible ZAB (Fig. 4e). To be specific, the flexible, bendable and stretchable PVA gel electrolyte could provide the flexible ZABs with the mechanical flexibility and the ionic conductivity. The open circuit voltage of the assembled flexible ZAB was

1.42 V, as measured with a multimeter, and the open circuit potential measured with an electrochemical workstation was 1.45 V, and it remained stable in 1200 s (Fig. 4f). The discharge curve of the solid-state ZAB indicated that, the corresponding current density at 1.0 V was 54.24 mA cm<sup>-2</sup>, and the corresponding power density reached 92.06 mW cm<sup>-2</sup> (Fig. 4g). According to Fig. 4h and h inset, the charge-discharge potential difference of the flexible ZAB under a current density of 5 mA cm<sup>-2</sup> was only 0.78 V, while the charge-discharge potential difference after 23 h (34.5 cycles) was 0.87 V, significantly comparable to the recent reported techniques (Table S2). To more specifically study its practical application, integrating two solid-state ZAB to a series circuit can light up a commercial red LED (~3 V). When the battery was bent to 0°, 90°, 120° and 180° in sequence, the light of the red LED could basically remain stable (Fig. 4i). As indicated from the results, the catalyst shows wide application prospects in rechargeable, flexible solid ZAB for wearable devices.

To investigate the ZAB reversibility and the particular effect of CoS<sub>2</sub>/Cu<sub>2</sub>S-NF air cathode, the in-situ characterizing approaches (ATR-FTIR, in-situ RAMAN and in-situ XRD) were adopted to capture the solid state under the working conditions. Fig. 5a presents the schematic diagram of the internal structure and chemical transformation of the ZAB. Here, ATR-FTIR was first performed to accurately investigate the adsorption and desorption of the transition state on the air cathode surface of the ZAB in the operation. When the \*O<sub>2</sub><sup>-</sup> form was adsorbed on the catalyst surface, the in-situ infrared spectrum shows a vibration peak of \*O<sub>2</sub><sup>-</sup> in the region of 1015–1180 cm<sup>-1</sup> [1,52]. The characteristic peak in 1400 cm<sup>-1</sup> was the O-O vibration peak of O<sub>2</sub> [53]. According to Fig. 5b and Fig. S11a, the characteristic peaks of \*O<sub>2</sub><sup>-</sup> and O<sub>2</sub> appeared and disappeared regularly as the battery was charged and discharged. The main reason was that with the battery charging, the in-situ infrared spectrum appeared. The vibration peak of \*O<sub>2</sub><sup>-</sup> appeared in the area close to 1180 cm<sup>-1</sup>. As the reaction progressed, \*O<sub>2</sub><sup>-</sup> was converted to O<sub>2</sub> and precipitated. The vibration peak of O-O with the characteristic peak of O<sub>2</sub> in the area of 1400 cm<sup>-1</sup> increased, while \*O<sub>2</sub><sup>-</sup> characteristic peak was obviously weakened to disappear, and the adsorbed O<sub>2</sub> was converted to \*O<sub>2</sub><sup>-</sup> as the reaction progressed. This figure visually indicates that the ZAB here exhibited the excellent electrocatalytic reaction performance in CoS<sub>2</sub>/Cu<sub>2</sub>S-NF air cathode.

For an in-depth assessment of the reaction system of the CoS<sub>2</sub>/Cu<sub>2</sub>S-NF air cathode, the in-situ Raman spectrum was continuously observed during the whole operation (Fig. 5c and Fig. S11b). The characteristic peak of ZnO appeared at 387 cm<sup>-1</sup>, and the concentration of zinc ions gradually increased as the battery was charged. The characteristic peak gradually disappeared with the discharge of the battery the peak at 732 cm<sup>-1</sup> was mainly the characteristic peak of CoS<sub>2</sub>/Cu<sub>2</sub>S-NF metal [54,55]. It could be clearly seen that the peak intensity of the characteristic peak increased and decreased regularly as the battery reaction progressed, and it lastly returned to the initial state. The main reason was that in the catalytic reaction, the adsorption and desorption of the surface material of the active center exerted a certain masking effect on the characteristic peak signal [11]. To verify the key role of CoS<sub>2</sub>/Cu<sub>2</sub>S-NF in the catalytic oxygen reaction, the in-situ test was performed on XRD phase change of CoS<sub>2</sub>/Cu<sub>2</sub>S-NF during the operation of the ZAB (Fig. 5d and Fig. S11c). According to the figure, with the progress of electrochemical charge and discharge, the characteristic peaks of CoS<sub>2</sub>/Cu<sub>2</sub>S-NF remained changed insignificantly. Besides, the individual peaks increased and decreased regularly, and lastly they returned to the original state. The mentioned result indicated that the adsorption and desorption of substances on the catalyst surface complied with the ORR and OER mechanism, and the change attributed to O<sub>2</sub> adsorption and desorption on the catalyst surface was completely reversible [56]. Moreover, it was confirmed that the material was stable under a wide working potential, which could be a vital condition for ensuring battery stability and has application value.

As indicated from the relevant theoretical studies on electrocatalytic

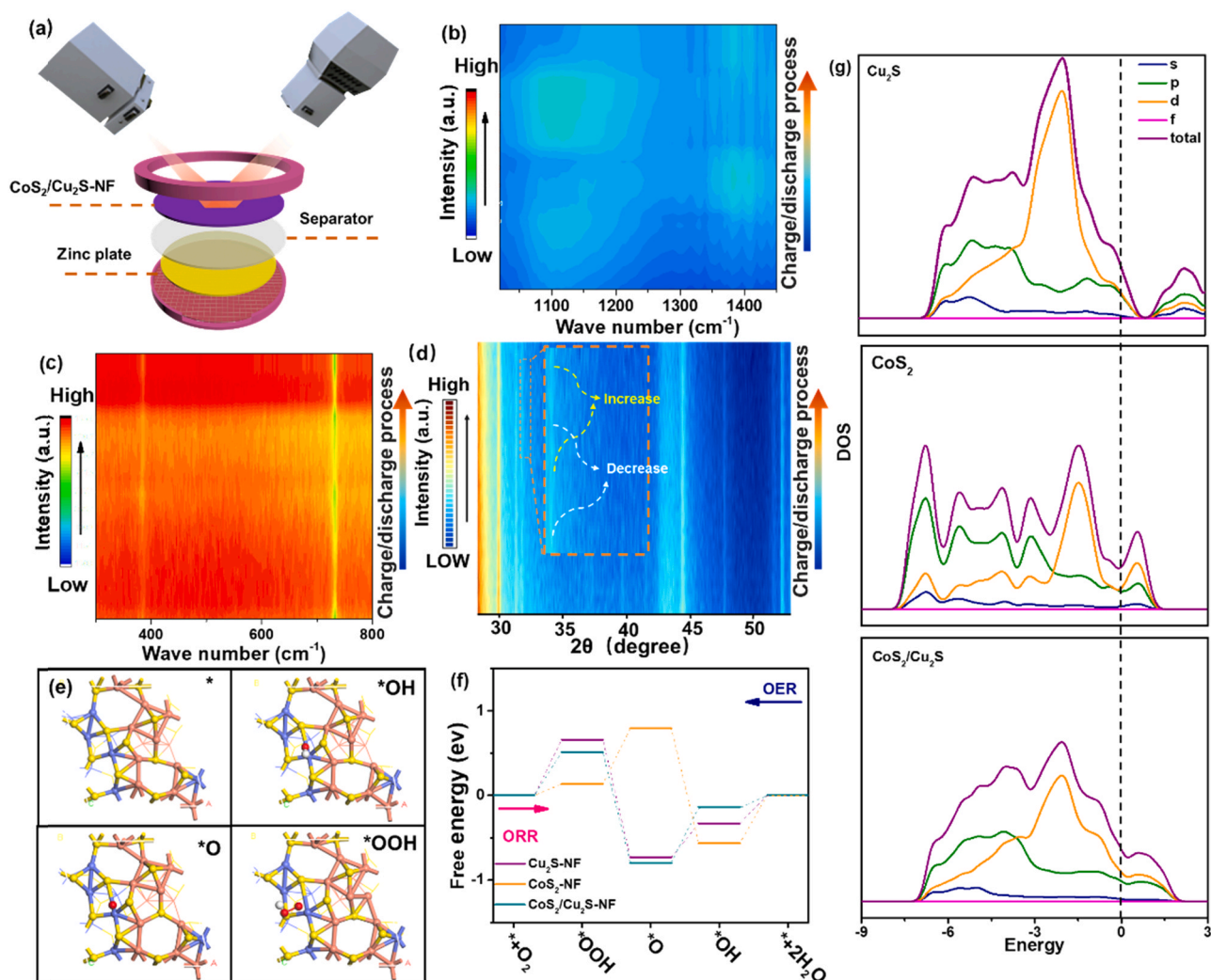


**Fig. 5.** (a) Schematic diagram of the in-situ characterization; (b) ATR-FTIR, (c) in-situ Raman and (d) In-situ XRD intensity map of ZAB with CoS<sub>2</sub>/Cu<sub>2</sub>S-NF electrodes during discharging and charging; (e) Local structural configurations of initial reactant, intermediates, or final product on the CoS<sub>2</sub>/Cu<sub>2</sub>S; (f) Free energy diagrams for Cu<sub>2</sub>S, CoS<sub>2</sub> and CoS<sub>2</sub>/Cu<sub>2</sub>S (The OER pathways are summarized at U = 1.23 V). (g) DOS of Cu<sub>2</sub>S, CoS<sub>2</sub> and CoS<sub>2</sub>/Cu<sub>2</sub>S (Black dashed line represents the Fermi level).

oxygen reactions (ORR and OER), the reaction activity was largely determined by the free energy of the intermediates (\*OH, \*O and \*OOH) on the catalyst surface. Fig. 5e presents the various bases of the electrocatalytic reaction of materials. As shown in Fig. 5f, the required energy of third step in the ORR process for CoS<sub>2</sub>/Cu<sub>2</sub>S is 0.644 eV, which is smaller than that the model of Cu<sub>2</sub>S (0.660 eV, from \*+O<sub>2</sub> to \*OOH) and CoS<sub>2</sub> (0.656 eV, from \*OH to \*O). This result reveals that the third step of ORR is the rate-determining step for CoS<sub>2</sub>/Cu<sub>2</sub>S. In the OER, the decisive step between CoS<sub>2</sub>/Cu<sub>2</sub>S and Cu<sub>2</sub>S was the conversion of \*OH and \*O, and their free energy differences reached 1.311 eV and 1.391 eV, respectively. However, the decisive step of the CoS<sub>2</sub> catalyzed oxygen reaction was the conversion of \*OH and \*O, and the free energy difference that should be overcome is 1.358 eV. The OER/ORR pathways are also summarized at U = 0 V, which is consistent with the original energy diagram under the equilibrium potential (Fig. S12). Compared with single metal sulfides, CoS<sub>2</sub>/Cu<sub>2</sub>S heterojunction could effectively optimize the decisive step of the catalytic reaction and enhance electrochemical activity [57]. It was therefore indicated the reaction energy barrier of the CoS<sub>2</sub>/Cu<sub>2</sub>S catalyst catalyzing the oxygen reaction was the smallest, which demonstrated that the interaction between CoS<sub>2</sub> and Cu<sub>2</sub>S heterostructure could effectively improve the conversion step. The electrocatalytic oxygen reaction exhibited the maximal catalytic activity. The theoretical calculation result was

consistent with the electrochemical test result. The electronic density of states (DOS) of CoS<sub>2</sub>, Cu<sub>2</sub>S and Cu<sub>2</sub>S/CoS<sub>2</sub> are presented in Fig. 5g. According to the figure, all DOS exhibited the metallic characteristics of materials, which enhanced the intrinsic conductivity. Compared with the density of states diagrams close to the Fermi level of CoS<sub>2</sub> and Cu<sub>2</sub>S, the peak of CoS<sub>2</sub>/Cu<sub>2</sub>S was gentler, which demonstrated that the electron delocalization of the heterostructure was stronger. Accordingly, the electron conduction could be facilitated, the electrocatalytic performance could be improved by promoting the effective electron transfer between the catalyst surface and the absorbed intermediate [45].

#### 4. Conclusions

In this study, the flexible self-supporting carbon nanofibers were adopted as the carrier to realize the load on the CoS<sub>2</sub>/Cu<sub>2</sub>S heterojunction. The carbon matrix effectively improved the conductivity of the material and protected the stability of the CoS<sub>2</sub>/Cu<sub>2</sub>S structure and phase. As indicated from the electrochemical tests, by using CoS<sub>2</sub>/Cu<sub>2</sub>S-NF as a bifunctional catalyst for oxygen reaction (ORR and OER), its reversible potential difference was only 0.73 V ( $\Delta E$ ), which demonstrated that the prepared CoS<sub>2</sub>/Cu<sub>2</sub>S-NF catalyst exhibited excellent electrocatalytic activity and a bifunctional catalytic ORR/OER

reversibility. When applied to a liquid ZAB, the specific capacity was  $812.78 \text{ mA h g}^{-1}$ , and the power density could reach  $260.60 \text{ mW cm}^{-2}$  at  $0.56 \text{ V}$ . After 350 h, 1050 charge-discharge cycles did not exhibit any significant performance degradation. Moreover, as a flexible self-supporting carrier, the material could act as an air electrode in a flexible ZAB. The obtained composite  $\text{CoS}_2/\text{Cu}_2\text{S-NF}$  exhibited its outstanding cycle stability (23 h charge-discharge stable cycle), high activity (power density of  $92.06 \text{ mW cm}^{-2}$ ) and high flexibility. This study considered that  $\text{CoS}_2/\text{Cu}_2\text{S-NF}$  could solve the defects of a single material and be employed in ZABs. Through the in-situ characterization methods (e.g., ATR-FTIR, in-situ RAMAN and in-situ XRD) integrated with DFT calculation demonstration, the active center of the material and the rate-determining step in the catalytic oxygen reaction activity were further determined. This study provided the valuable ideas and solutions for the further optimized design of this type of catalyst in the future.

### CRedit authorship contribution statement

**Wanqing Li:** Conducting experiments, Writing. **Lei Wu:** Data Analysis. **Xiaochao Wu:** Data Analysis. **Chuan Shi:** Conducting Characterization. **Yongliang Li:** Data Analysis, Editing. **Lei Zhang:** Data Analysis, Editing. **Hongwei Mi:** Data Analysis. **Qianling Zhang:** Method Development. **Chuanxin He:** Data Analysis. **Xiangzhong Ren:** Supervision, Editing.

### Declaration of Competing Interest

The authors declare that they have no known competing financial interests or personal relationships that could have appeared to influence the work reported in this paper.

### Acknowledgements

This work was financially supported by the National Natural Science Foundation of China (21671136), Guangdong Basic and Applied Basic Research Foundation (2020A151010379), Project of Educational Commission of Guangdong Province of China (2020ZDZX2011), Shenzhen Science and Technology Project Program (JCYJ20190808144413257, JCYJ20190808145203535), Shenzhen Key Projects of Technological Research (JSGG20200925145800001), the China Postdoctoral Science Foundation (2019M663074) and Instrumental Analysis Center of Shenzhen University.

### Appendix A. Supporting information

Supplementary data associated with this article can be found in the online version at [doi:10.1016/j.apcatb.2021.120849](https://doi.org/10.1016/j.apcatb.2021.120849).

### References

- W. Li, Y. Li, H. Fu, G. Yang, Q. Zhang, S. Chen, F. Peng, Phosphorus doped  $\text{Co}_3\text{S}_8$ @CS as an excellent air-electrode catalyst for zinc-air batteries, *Chem. Eng. J.* 381 (2020), 122683, <https://doi.org/10.1016/j.cej.2019.122683>.
- K. Tang, C. Yuan, Y. Xiong, H. Hu, M. Wu, Inverse-opal-structured hybrids of N, S-codoped-carbon-confined  $\text{Co}_3\text{S}_8$  nanoparticles as bifunctional oxygen electrocatalyst for on-chip all-solid-state rechargeable Zn-air batteries, *Appl. Catal. B: Environ.* 260 (2020), 118209, <https://doi.org/10.1016/j.apcatb.2019.118209>.
- Y. Guan, Y. Li, S. Luo, X. Ren, L. Deng, L. Sun, H. Mi, P. Zhang, J. Liu, Rational design of positive-hexagon-shaped two-dimensional ZIF-derived materials as improved bifunctional oxygen electrocatalysts for use as long-lasting rechargeable Zn-Air batteries, *Appl. Catal. B: Environ.* 256 (2019), 117871, <https://doi.org/10.1016/j.apcatb.2019.117871>.
- X. Zhao, H. Cheng, L. Song, L. Han, R. Zhang, G. Kwon, L. Ma, S.N. Ehrlich, A. I. Frenkel, J. Yang, K. Sasaki, H.L. Xin, Rhombohedral ordered intermetallic nanocatalyst boosts the oxygen reduction reaction, *ACS Catal.* 11 (2020) 184–192, <https://doi.org/10.1021/acscatal.0c04021>.
- J. Ding, S. Ji, H. Wang, B.G. Pollet, R. Wang, Mesoporous  $\text{CoS}/\text{N}$ -doped carbon as HER and ORR bifunctional electrocatalyst for water electrolyzers and Zinc-air batteries, *ChemCatChem* 11 (2019) 1026–1032, <https://doi.org/10.1002/cctc.201801618>.
- J. Bai, T. Meng, D. Guo, S. Wang, B. Mao, M. Cao,  $\text{Co}_3\text{S}_8/\text{MoS}_2$  core-shell heterostructures as trifunctional electrocatalysts for overall water splitting and Zn-air batteries, *ACS Appl. Mater. Interfaces* 10 (2018) 1678–1689, <https://doi.org/10.1021/acsaami.7b14997>.
- S. Cui, X. Liu, Z. Sun, P. Du, Noble metal-free copper hydroxide as an active and robust electrocatalyst for water oxidation at weakly basic pH, *ACS Sustain. Chem. Eng.* 4 (2016) 2593–2600, <https://doi.org/10.1021/acsschemeng.6b00067>.
- R. Lin, S.M. Bak, Y. Shin, R. Zhang, C. Wang, K. Kisslinger, M. Ge, X. Huang, Z. Shadike, A. Pattammattel, H. Yan, Y. Chu, J. Wu, W. Yang, M.S. Whittingham, H. L. Xin, X.Q. Yang, Hierarchical nickel valence gradient stabilizes high-nickel content layered cathode materials, *Nat. Commun.* 12 (2021) 2350, <https://doi.org/10.1038/s41467-021-22635-w>.
- M.H. Seo, H.W. Park, D.U. Lee, M.G. Park, Z. Chen, Design of highly active perovskite oxides for oxygen evolution reaction by combining experimental and ab initio studies, *ACS Catal.* 5 (2015) 4337–4344, <https://doi.org/10.1021/acscatal.5b00114>.
- H. Lei, Z. Wang, F. Yang, X. Huang, J. Liu, Y. Liang, J. Xie, M.S. Javed, X. Lu, S. Tan, W. Mai, NiFe nanoparticles embedded N-doped carbon nanotubes as high-efficient electrocatalysts for wearable solid-state Zn-air batteries, *Nano Energy* 68 (2020), 104293, <https://doi.org/10.1016/j.nanoen.2019.104293>.
- H. Ji, M. Wang, S. Liu, H. Sun, J. Liu, T. Qian, C. Yan, Pyridinic and graphitic nitrogen-enriched carbon paper as a highly active bifunctional catalyst for Zn-air batteries, *Electrochim. Acta* 334 (2020), 135562, <https://doi.org/10.1016/j.electacta.2019.135562>.
- H. Xu, J. Cao, C. Shan, B. Wang, P. Xi, W. Liu, Y. Tang, MOF-derived hollow  $\text{CoS}$  decorated with  $\text{FeO}_x$  nanoparticles for boosting oxygen evolution reaction electrocatalysis, *Angew. Chem. Int. Ed.* 57 (2018) 8654–8658, <https://doi.org/10.1002/anie.201804673>.
- T. Li, G. Luo, K. Liu, X. Li, D. Sun, L. Xu, Y. Li, Y. Tang, Encapsulation of  $\text{Ni}_3\text{Fe}$  nanoparticles in N-doped carbon nanotube-grafted carbon nanofibers as high-efficiency hydrogen evolution electrocatalysts, *Adv. Funct. Mater.* 28 (2018), 1805828, <https://doi.org/10.1002/adfm.201805828>.
- X. Cao, E. Johnson, M. Nath, Expanding multinary selenide based high-efficiency oxygen evolution electrocatalysts through combinatorial electrodeposition: case study with Fe-Cu-Co selenides, *ACS Sustain. Chem. Eng.* 7 (2019) 9588–9600, <https://doi.org/10.1021/acssuschemeng.9b01095>.
- G. Nam, J. Park, M. Choi, P. Oh, S. Park, M.G. Kim, N. Park, J. Cho, J.S. Lee, Carbon-coated core-shell Fe-Cu nanoparticles as highly active and durable electrocatalysts for a Zn-air battery, *ACS Nano* 9 (2015) 6493–6501, <https://doi.org/10.1021/acsnano.5b02266>.
- C.Y. Su, H. Cheng, W. Li, Z.Q. Liu, N. Li, Z. Hou, F.Q. Bai, H.X. Zhang, T.Y. Ma, Atomic modulation of FeCo-nitrogen-carbon bifunctional oxygen electrodes for rechargeable and flexible all-solid-state zinc-air battery, *Adv. Energy Mater.* 7 (2017), 1602420, <https://doi.org/10.1002/aenm.201602420>.
- S.K. Singh, V. Kashyap, N. Manna, S.N. Bhange, R. Soni, R. Boukherroub, S. Szunerits, S. Kurungot, Efficient and durable oxygen reduction electrocatalyst based on CoMn alloy oxide nanoparticles supported over N-doped porous graphene, *ACS Catal.* 7 (2017) 6700–6710, <https://doi.org/10.1021/acscatal.7b01983>.
- X. Chen, C. Zhong, B. Liu, Z. Liu, X. Bi, N. Zhao, X. Han, Y. Deng, J. Lu, W. Hu, Atomic layer  $\text{Co}_3\text{O}_4$  nanosheets: the key to knittable Zn-air batteries, *Small* 14 (2018), e1702987, <https://doi.org/10.1002/sml.201702987>.
- R. Jin, J. Zhou, Y. Guan, H. Liu, G. Chen, Mesocrystal  $\text{Co}_3\text{S}_8$  hollow sphere anodes for high performance lithium ion batteries, *J. Mater. Chem. A* 2 (2014) 13241–13244, <https://doi.org/10.1039/c4ta02551b>.
- J. Du, Z. Chen, S. Ye, B.J. Wiley, T.J. Meyer, Copper as a robust and transparent electrocatalyst for water oxidation, *Angew. Chem. Int. Ed. Engl.* 54 (2015) 2073–2078, <https://doi.org/10.1002/anie.201408854>.
- Y. Gao, N. Zhang, C. Wang, F. Zhao, Y. Yu, Construction of  $\text{Fe}_2\text{O}_3/\text{CuO}$  heterojunction nanotubes for enhanced oxygen evolution reaction, *ACS Appl. Energy Mater.* 3 (2019) 666–674, <https://doi.org/10.1021/acsaem.9b01866>.
- P. Zou, R. Zhang, L. Yao, J. Qin, K. Kisslinger, H. Zhuang, H.L. Xin, Ultrahigh-rate and long-life zinc-metal anodes enabled by self-accelerated cation migration, *Adv. Energy Mater.* 11 (2021), <https://doi.org/10.1002/aenm.202100982>.
- S. Huang, Y. Meng, S. He, A. Goswami, Q. Wu, J. Li, S. Tong, T. Asefa, M. Wu, N-, O-, and S-tridoped carbon-encapsulated  $\text{Co}_3\text{S}_8$  nanomaterials: Efficient bifunctional electrocatalysts for overall water splitting, *Adv. Funct. Mater.* 27 (2017), 1606585, <https://doi.org/10.1002/adfm.201606585>.
- X. Zheng, X. Han, Y. Cao, Y. Zhang, D. Nordlund, J. Wang, S. Chou, H. Liu, L. Li, C. Zhong, Y. Deng, W. Hu, Identifying dense  $\text{NiSe}_2/\text{CoSe}_2$  heterointerfaces coupled with surface high-valence bimetallic sites for synergistically enhanced oxygen electrocatalysis, *e2000607*, *Adv. Mater.* 32 (2020), 2000607, <https://doi.org/10.1002/adma.202000607>.
- K. Wu, L. Zhang, Y. Yuan, L. Zhong, Z. Chen, X. Chi, H. Lu, Z. Chen, R. Zou, T. Li, C. Jiang, Y. Chen, X. Peng, J. Lu, An iron-decorated carbon aerogel for rechargeable flow and flexible Zn-air batteries, *e2002292*, *Adv. Mater.* 32 (2020), 2002292, <https://doi.org/10.1002/adma.202002292>.
- Q. Lu, H. Wu, X. Zheng, Y. Chen, A.L. Rogach, X. Han, Y. Deng, W. Hu, Encapsulating cobalt nanoparticles in interconnected N-doped hollow carbon nanofibers with enriched CoNC moiety for enhanced oxygen electrocatalysis in Zn-air batteries, *e2101438*, *Adv. Sci.* 8 (2021), 2101438, <https://doi.org/10.1002/advs.202101438>.
- F. Dionigi, Z. Zeng, I. Sinev, T. Merzdorf, S. Deshpande, M.B. Lopez, S. Kunze, I. Zegkinoglou, H. Sarodnik, D. Fan, A. Bergmann, J. Drnec, J.F. Araujo, M. Gliech,



- D. Teschner, J. Zhu, W.X. Li, J. Greeley, B.R. Cuenya, P. Strasser, In-situ structure and catalytic mechanism of NiFe and CoFe layered double hydroxides during oxygen evolution, *Nat. Commun.* 11 (2020) 2522, <https://doi.org/10.1038/s41467-020-16237-1>.
- [28] X. Wei, X. Wang, Q. An, C. Han, L. Mai, Operando X-ray diffraction characterization for understanding the intrinsic electrochemical mechanism in rechargeable battery materials, *Small Methods* 1 (2017), 1700083, <https://doi.org/10.1002/smt.201700083>.
- [29] W. Li, D. Wang, Y. Zhang, L. Tao, T. Wang, Y. Zou, Y. Wang, R. Chen, S. Wang, Defect engineering for fuel-cell electrocatalysts, *Adv. Mater.* 32 (2020), 1907879, <https://doi.org/10.1002/adma.201907879>.
- [30] J. Hu, Y. Chu, Q. Tian, J. Wang, Y. Li, Q. Wu, L. Zhao, Y. Zhu, Film cathode for thermal batteries using a screen-printing process, *Mater. Lett.* 215 (2018) 296–299, <https://doi.org/10.1016/j.matlet.2017.12.114>.
- [31] N. Shi, B. Xi, M. Huang, X. Ma, H. Li, J. Feng, S. Xiong, Hierarchical octahedra constructed by  $\text{Cu}_2\text{S}/\text{MoS}_2$  subset carbon framework with enhanced sodium storage, *Small* 16 (2020), 2000952, <https://doi.org/10.1002/sml.202000952>.
- [32] S. Dang, Q.-L. Zhu, Q. Xu, Nanomaterials derived from metal-organic frameworks, *Nat. Rev. Mater.* 3 (2017) 1701, <https://doi.org/10.1038/natrevmats.2017.75>.
- [33] S. Foley, H. Geaney, G. Bree, K. Stokes, S. Connolly, M.J. Zaworotko, K.M. Ryan, Copper sulfide ( $\text{Cu}_2\text{S}$ ) nanowire-in-carbon composites formed from direct sulfurization of the metal-organic framework HKUST-1 and their use as Li-ion battery cathodes, *Adv. Funct. Mater.* 28 (2018), 1800587, <https://doi.org/10.1002/adfm.201800587>.
- [34] X. Han, X. Wu, C. Zhong, Y. Deng, N. Zhao, W. Hu,  $\text{NiCo}_2\text{S}_4$  nanocrystals anchored on nitrogen-doped carbon nanotubes as a highly efficient bifunctional electrocatalyst for rechargeable zinc-air batteries, *Nano Energy* 31 (2017) 541–550, <https://doi.org/10.1016/j.nanoen.2016.12.008>.
- [35] W. Li, Y. Li, H. Wang, Y. Cao, H. Yu, F. Peng,  $\text{CoS}_x$ -porous carbon spheres as bifunctional electrocatalysts with high activity and stability for oxygen reduction and evolution reactions, *Electrochim. Acta* 265 (2018) 32–40, <https://doi.org/10.1016/j.electacta.2018.01.095>.
- [36] Y. Tian, L. Xu, M. Li, D. Yuan, X. Liu, J. Qian, Y. Dou, J. Qiu, S. Zhang, Interface engineering of  $\text{CoS}/\text{CoO}@N$ -doped graphene nanocomposite for high-performance rechargeable Zn-air batteries, *Nano-Micro Lett.* 13 (2020) 3, <https://doi.org/10.1007/s40820-020-00526-x>.
- [37] D.C. Nguyen, D.T. Tran, T.L.L. Doan, D.H. Kim, N.H. Kim, J.H. Lee, Rational design of core@shell structured  $\text{CoS}_x@Cu_2MoS_4$  hybridized  $\text{MoS}_2/N$ -codoped graphene as advanced electrocatalyst for water splitting and Zn-air battery, *Adv. Energy Mater.* 10 (2020), 1903289, <https://doi.org/10.1002/aenm.201903289>.
- [38] L. Yan, Z. Xu, W. Hu, J. Ning, Y. Zhong, Y. Hu, Formation of sandwiched leaf-like CNTs- $\text{Co}/\text{ZnCo}_2\text{O}_4@NC$ -CNTs nanohybrids for high-power-density rechargeable Zn-air batteries, *Nano Energy* 82 (2021), 105710, <https://doi.org/10.1016/j.nanoen.2020.105710>.
- [39] F. Pan, Z. Li, Z. Yang, Q. Ma, M. Wang, H. Wang, M. Olszta, G. Wang, Z. Feng, Y. Du, Y. Yang, Porous FeCo glassy alloy as bifunctional support for high-performance Zn-air battery, *Adv. Energy Mater.* 11 (2020), 2002204, <https://doi.org/10.1002/aenm.202002204>.
- [40] H. Zhang, Z. Yang, X. Wang, S. Yan, T. Zhou, C. Zhang, S.G. Telfer, S. Liu, Uniform copper-cobalt phosphides embedded in N-doped carbon frameworks as efficient bifunctional oxygen electrocatalysts for rechargeable Zn-air batteries, *Nanoscale* 11 (2019) 17384–17395, <https://doi.org/10.1039/c9nr04837e>.
- [41] H.F. Wang, C. Tang, B. Wang, B.Q. Li, Q. Zhang, Bifunctional transition metal hydroxysulfides: room-temperature sulfurization and their applications in Zn-Air batteries, *Adv. Mater.* 29 (2017), 1702327, <https://doi.org/10.1002/adma.201702327>.
- [42] L. An, Y. Li, M. Luo, J. Yin, Y.Q. Zhao, C. Xu, F. Cheng, Y. Yang, P. Xi, S. Guo, Atomic-Level coupled interfaces and lattice distortion on  $\text{CuS}/\text{NiS}_2\text{N}$  anocrystals boost oxygen catalysis for flexible Zn-air batteries, *Adv. Funct. Mater.* 27 (2017), 1703779, <https://doi.org/10.1002/adfm.201703779>.
- [43] C. Guo, Y. Zheng, J. Ran, F. Xie, M. Jaroniec, S.Z. Qiao, Engineering high-energy interfacial structures for high-Performance oxygen-involving electrocatalysis, *Angew. Chem. Int. Ed.* 56 (2017) 8539–8543, <https://doi.org/10.1002/anie.201701531>.
- [44] B. Li, X. Ge, F.W. Goh, T.S. Hor, D. Geng, G. Du, Z. Liu, J. Zhang, X. Liu, Y. Zong,  $\text{Co}_3\text{O}_4$  nanoparticles decorated carbon nanofiber mat as binder-free air-cathode for high performance rechargeable Zinc-air batteries, *Nanoscale* 7 (2015) 1830–1838, <https://doi.org/10.1039/c4nr05988c>.
- [45] X. He, Y. Tian, Z. Huang, L. Xu, J. Wu, J. Qian, J. Zhang, H. Li, Engineering the electronic states of  $\text{Ni}_3\text{FeN}$  via zinc ion regulation for promoting oxygen electrocatalysis in rechargeable Zn-air batteries, *J. Mater. Chem. A* 9 (2021) 2301–2307, <https://doi.org/10.1039/d0ta10370e>.
- [46] X. Zheng, B. Zhang, P. De Luna, Y. Liang, R. Comin, O. Voznyy, L. Han, F.P. Garcia de Arquer, M. Liu, C.T. Dinh, T. Regier, J.J. Dynes, S. He, H.L. Xin, H. Peng, D. Prendergast, X. Du, E.H. Sargent, Theory-driven design of high-valence metal sites for water oxidation confirmed using in situ soft X-ray absorption, *Nat. Chem.* 10 (2018) 149–154, <https://doi.org/10.1038/nchem.2886>.
- [47] R. Luo, Z. Qian, L. Xing, C. Du, G. Yin, S. Zhao, L. Du, Re-looking into the active moieties of metal X-ides (X=phosph-, sulf-, nit-, and carb-) toward oxygen evolution reaction, *Adv. Funct. Mater.* 31 (2021), 2102918, <https://doi.org/10.1002/adfm.202102918>.
- [48] Y. Zuo, Y. Liu, J. Li, R. Du, X. Han, T. Zhang, J. Arbiol, N.J. Divins, J. Llorca, N. Guijarro, K. Sivula, A. Cabot, In situ electrochemical oxidation of  $\text{Cu}_2\text{S}$  into  $\text{CuO}$  nanowires as a durable and efficient electrocatalyst for oxygen evolution reaction, *Chem. Mater.* 31 (2019) 7732–7743, <https://doi.org/10.1021/acs.chemmater.9b02790>.
- [49] P. Cai, J. Huang, J. Chen, Z. Wen, Oxygen-containing amorphous cobalt sulfide porous nanocubes as high-activity electrocatalysts for the oxygen evolution reaction in an alkaline/neutral medium, *Angew. Chem.* 129 (2017) 4936–4939, <https://doi.org/10.1002/ange.201701280>.
- [50] L. An, Y. Li, M. Luo, J. Yin, Y.Q. Zhao, C. Xu, F. Cheng, Y. Yang, P. Xi, L. Guo, Atomic-level coupled interfaces and lattice distortion on  $\text{CuS}/\text{NiS}_2$  nanocrystals boost oxygen catalysis for flexible Zn-air batteries, *Adv. Funct. Mater.* 27 (2017), 1703779, <https://doi.org/10.1002/adfm.201703779>.
- [51] J. Jiang, S. Lu, W.K. Wang, G.X. Huang, B.C. Huang, F. Zhang, Y.-J. Zhang, H. Q. Yu, Ultrahigh electrocatalytic oxygen evolution by iron-nickel sulfide nanosheets/reduced graphene oxide nanohybrids with an optimized autoxidation process, *Nano Energy* 43 (2018) 300–309, <https://doi.org/10.1016/j.nanoen.2017.11.049>.
- [52] M.W. Li, M.H. Fu, Y. Cao, H. Wang, H. Yu, Z. Qiao, H. Liang, F. Peng,  $\text{Mn}_3\text{O}_4@C$  nanoparticles supported on porous carbon as bifunctional oxygen electrodes and their electrocatalytic mechanism, *ChemElectroChem* 6 (2019) 359–368, <https://doi.org/10.1002/celec.201801464>.
- [53] K. Kunimatsu, T. Yoda, D.A. Tryk, H. Uchida, M. Watanabe, In situ ATR-FTIR study of oxygen reduction at the Pt/Nafion interface, *Phys. Chem. Chem. Phys.* 12 (2010) 621–629, <https://doi.org/10.1039/b917306d>.
- [54] M. Hansen, J. Truong, T. Xie, J.I. Hahn, Spatially distinct Raman scattering characteristics of individual ZnO nanorods under controlled polarization: intense end scattering from forbidden modes, *Nanoscale* 9 (2017) 8470–8480, <https://doi.org/10.1039/c7nr02672b>.
- [55] S. Liu, M. Wang, X. Sun, N. Xu, J. Liu, Y. Wang, T. Qian, C. Yan, Facilitated oxygen chemisorption in heteroatom-doped carbon for improved oxygen reaction activity in all-solid-state Zinc-air batteries, *Adv. Mater.* 30 (2018), 1704898, <https://doi.org/10.1002/adma.201704898>.
- [56] H. Ji, M. Wang, S. Liu, H. Sun, J. Liu, T. Qian, C. Yan, In-situ observation as activity descriptor enables rational design of oxygen reduction catalyst for zinc-air battery, *Energy Storage Mater.* 27 (2020) 226–231, <https://doi.org/10.1016/j.ensm.2020.02.002>.
- [57] H.J. Qiu, P. Du, K. Hu, J. Gao, H. Li, P. Liu, T. Ina, K. Ohara, Y. Ito, M. Chen, Metal and nonmetal codoped 3D nanoporous graphene for efficient bifunctional electrocatalysis and rechargeable Zn-Air batteries, *Adv. Mater.* 31 (2019), 1900843, <https://doi.org/10.1002/adma.201900843>.